nature communications

Article

https://doi.org/10.1038/s41467-024-53474-0

Restructuring the interfacial active sites to generalize the volcano curves for platinum-cobalt synergistic catalysis

Received: 29 March 2024

Accepted: 11 October 2024

Wenyao Chen[1,5], Yao Shi[1,5], Changwei Liu[1,5], Zhouhong Ren[2,5], Zikun Huang[1], Zhou Chen[1], Xiangxue Zhang[1], Shanshan Liang[1], Lei Xie[3], Cheng Lian[1] ✉, Gang Qian[1], Jing Zhang[1], Xi Liu[2] ✉, De Chen[4], Xinggui Zhou[1], Weikang Yuan[1] & Xuezhi Duan[1] ✉

Computationally derived volcano curve has become the gold standard in catalysis, whose practical application usually relies on empirical interpretations of composition or size effects by the identical active site assumption. Here, we present a proof-of-concept study on disclosing both the support- and adsorbate-induced restructuring of Pt-Co bimetallic catalysts, and the related interplays among different interfacial sites to propose the synergy-dependent volcano curves. Multiple characterizations, isotopic kinetic investigations, and multiscale simulations unravel that the progressive incorporation of Co into Pt catalysts, driven by strong Pt-C bonding (metal-support interfaces) and Co-O bonding (metal-adsorbate interfaces), initiates the formation of Pt-rich alloys accompanied by isolated Co species, then Co segregation to epitaxial CoO_x overlayers and adjacent Co_3O_4 clusters, and ultimately structural collapse into amorphous alloys. Accordingly, three distinct synergies, involving lattice oxygen redox from Pt-Co alloy/Co_3O_4 clusters, dual-active sites engineering via Pt-rich alloy/CoO_x overlayer, and electron coupling within exposed alloy, are identified and quantified for CO oxidation (gas-phase), ammonia borane hydrolysis (liquid-phase), and hydrogen evolution reaction (electrocatalysis), respectively. The resultant synergy-dependent volcano curves represent an advancement over traditional composition-/size-dependent ones, serving as a bridge between theoretical models and experimental observations in bimetallic catalysis.

Platinum (Pt) catalysts have been extensively studied and utilized across a wide range of applications involving energy conversion and environmental remediation[1–3]. Among them, Pt-based bimetallic materials stand out by virtue of their unique catalytic properties as well as relatively low cost via the introduction of a second metal component[4,5]. Significant efforts have been dedicated over the past decades to understanding how reactions are influenced by bimetallic materials and how to maximize catalytic activity[6,7]. Despite the well-

---

[1]State Key Laboratory of Chemical Engineering, East China University of Science and Technology, Shanghai, China. [2]School of Chemistry and Chemical Engineering, In-situ Center for Physical Sciences, Shanghai Jiao Tong University, Shanghai, China. [3]Shanghai Synchrotron Radiation Faciality, Shanghai Advanced Research Institute, Chinese Academy of Sciences, Shanghai, China. [4]Department of Chemical Engineering, Norwegian University of Science and Technology, Trondheim, Norway. [5]These authors contributed equally: Wenyao Chen, Yao Shi, Changwei Liu, Zhouhong Ren.
✉e-mail: liancheng@ecust.edu.cn; liuxi@sjtu.edu.cn; xzduan@ecust.edu.cn

recognized changes in chemistry, morphology, and energy observed on bimetallic surfaces in relative to either of the parent metal surfaces, predicting the modifications in geometric and electronic properties of Pt-based bimetallic surfaces and their resultant catalytic properties still remains challenging[8]. This is because the number and type of active sites, as well as their associated synergies on the bimetallic surface, are usually complex and difficult to know a priori, as they are flexible and can be modified drastically with environment[9–11]. Hence, the rational design and development of efficient Pt-based bimetallic catalysts necessitate a deep understanding of the diversified active sites over bimetallic surfaces and their underlying interplays under various preparation and reaction conditions, whose mesokinetics research is the ingress to bridge the microscopic-to-macroscopic transition in energy and environmental catalysis[12].

Volcano curve has become the gold standard in bimetallic catalyst design, which provides a straightforward guidance for optimizing catalytic performance by tuning the adsorption energies of reaction species[13–15]. Further combining the Sabatier principle, which emphasizes the importance of intermediate bonding neither being too strong nor too weak, we can gain systematic and intuitive explanations for the composition-/size-dependent volcano curves commonly observed in bimetallic catalysis[16,17]. The idea of moderate bonding suggested by the Sabatier principle is no doubt illumining, while the interpretations of the volcano curve derived from experience and commonsense are sometimes inconclusive and even contradictory. Exemplified by the widely studied Pt–Co bimetallic catalyst in previous studies on the same catalytic reaction, such as CO oxidation[18,19], ammonia borane hydrolysis[20–22], and hydrogen evolution reaction (HER)[23–25], contradictions arise as some recommend structures rich in Pt and poor in Co based on their reported volcano curves, while others advocate structures poor in Pt and rich in Co. Rationally, each bimetallic catalytic material has different optimal active sites in terms of their synergistic promotions, which is unlike the traditional volcano curves constructed by assuming the same active site for all materials[26]. Therefore, it is highly desirable to reevaluate these composition-/size-dependent volcano curves, and uncover the intricate synergies underlying different active sites for obtaining a more comprehensive and unified guiding principle.

Inspired by the above two concepts of active site and volcano curve for bimetallic catalysis, here we made an advance in disclosing the atomic-scale restructuring of Pt–Co bimetallic catalysts induced by support and adsorbate, and the related interplays among different interfacial sites to propose the synergy-dependent volcano curves. Exemplified by the mentioned three representative yet disputed reactions, namely CO oxidation (gas-phase), ammonia borane hydrolysis (liquid-phase), and hydrogen evolution reaction (electrocatalysis), a series of Pt–Co bimetallic catalysts with different compositions and sizes were prepared, whose catalytic activity can be similarly correlated with either the catalyst composition or size by volcano curves as previous studies. A combination of microscopic and spectroscopic characterization, multiscale simulation, isotopic labeling, and steady state isotopic transient kinetic analysis (SSITKA) was employed to unveil the atomic-scale restructuring concerning both site activity and surface stability. Further integrating the related mechanistic investigation, the most active yet stable synergies are identified and quantified to establish the synergy-dependent volcano curves. In comparison to the traditional composition-/size-dependent volcano curves based on the same active site assumption, the synergy-dependent volcano curves shed more insights into the interplays among different interfacial sites to bridge the gap between theoretical models and experimental observations in bimetallic catalysis.

Results

Composition-/size-dependent volcano curves

Platelet carbon nanofibers (CNF) with tunable surface chemistry, high electron conductivity, and large surface area were prepared by catalytic chemical vapor deposition (CCVD) and employed as catalyst support. Their supported Pt–Co bimetallic catalysts with the same Pt loading of 0.75 wt% while different molar ratios (n_{Pt}:n_{Co}) of 1:0, 1:1, 1:3, 1:5, and 1:7 were prepared and denoted as Pt/CNF, $PtCo_1$/CNF, $PtCo_3$/CNF, $PtCo_5$/CNF, and $PtCo_7$/CNF, respectively. The HAADF-STEM micrographs of the Pt/CNF catalyst depicted in Supplementary Fig. S1 demonstrate a homogeneous dispersion of metal particles, attributed to the abundant surface defects of CNF that serve as nucleation sites for metal immobilization. Upon Co incorporation, as illustrated in Supplementary Figs. S2–-S5, minor nanoparticle agglomeration is discernible, escalating markedly in bimetallic catalysts with elevated Co content, particularly for the $PtCo_7$/CNF catalyst. Consequently, the corresponding average metal particle size can be estimated based on the measurements of more than 200 random particles as 1.2 ± 0.3, 1.3 ± 0.4, 1.7 ± 0.4, 1.9 ± 0.4, and 2.5 ± 0.5 nm, respectively.

As shown in Fig. 1a, these catalysts were tested for three representative reactions, including CO oxidation (gas-phase), ammonia borane hydrolysis (liquid-phase), and hydrogen evolution reaction (electrocatalysis). It can be seen in Fig. 1b that, for CO oxidation, these catalysts deliver different conversions of CO at identical reaction conditions. As summarized in Fig. 1a, $PtCo_5$/CNF exhibits the highest catalytic activity of 129.6 $mmol_{CO}\cdot mol_{Pt}^{-1}\cdot s^{-1}$ at 140 °C, which is nearly 20 times higher than that of Pt/CNF. As can be seen in Supplementary Fig. S6, both the composition and size of these catalysts affect this reaction, and the former one can also be correlated with the catalytic activity by volcano curves. In Fig. 1c for ammonia borane hydrolysis, the addition of Co to Pt/CNF increases the initial hydrogen generation rate ($r_{initial}$) up to a maximum at $PtCo_3$/CNF, beyond which the reaction was inhibited. As shown in Fig, 1a, $PtCo_3$/CNF has more than two times the activity of Pt/CNF, and the catalytic activity can be also correlated with the composition by volcano curve in Supplementary Fig. S7. The Arrhenius plots presented in Supplementary Fig. S8 reveal that bimetallic catalysts possess lower activation energies compared to the monometallic Pt/CNF catalyst. Notably, the $PtCo_3$/CNF catalyst exhibits an optimal balance between activation energy and the pre-exponential factor, suggesting a finely tuned catalytic performance. For HER under Ar-saturated 1 M KOH solution as shown in Fig. 1d, bimetallic $PtCo_x$/CNF catalysts exhibit higher HER performances than monometallic Pt/CNF, and the overpotential of $PtCo_1$/CNF is much lower than that of Pt/CNF at the same current density. The corresponding Tafel plots and Nyquist plots are also given in Supplementary Figs. S9 and S10, respectively. As a result, the mass activity that normalized all the samples to the Pt loading at the same overpotential ($\eta = 0.35$ V) still demonstrates the composition-dependent volcano curve in Supplementary Fig. S11. Furthermore, it is observed that the monometallic Co/CNF catalyst displayed negligible catalytic activity across the three reactions.

Structural characterization and identification

It is obvious that the catalytic activity for these three reactions can be similarly correlated with either the composition or size of bimetallic catalysts as previous studies. Generally, the composition effects usually referred to their electronic properties in relation to the intrinsic activity of each active site, such as ligand and strain effects[7,27], while the size effects referred to their geometric properties in relation to the number of active sites, such as ensemble and steric effects[28,29]. The above two factors are not mutually exclusive, and if enhanced simultaneously, catalytic efficiency can be greatly improved, which is vice versa. In this regard, the electronic and geometric properties of these catalysts were characterized. The XRD patterns in Fig. 2a are almost identical for these catalysts and mainly exhibit diffraction peaks at 26.4°, 42.2°, 44.4°, and 54.5° ascribed to CNF support, and the absences of those ascribed to Pt and Co as well as their oxides are consistent with their low loadings and high dispersions as shown in HAADF-STEM images. In comparison, the H_2-TPR profiles vary

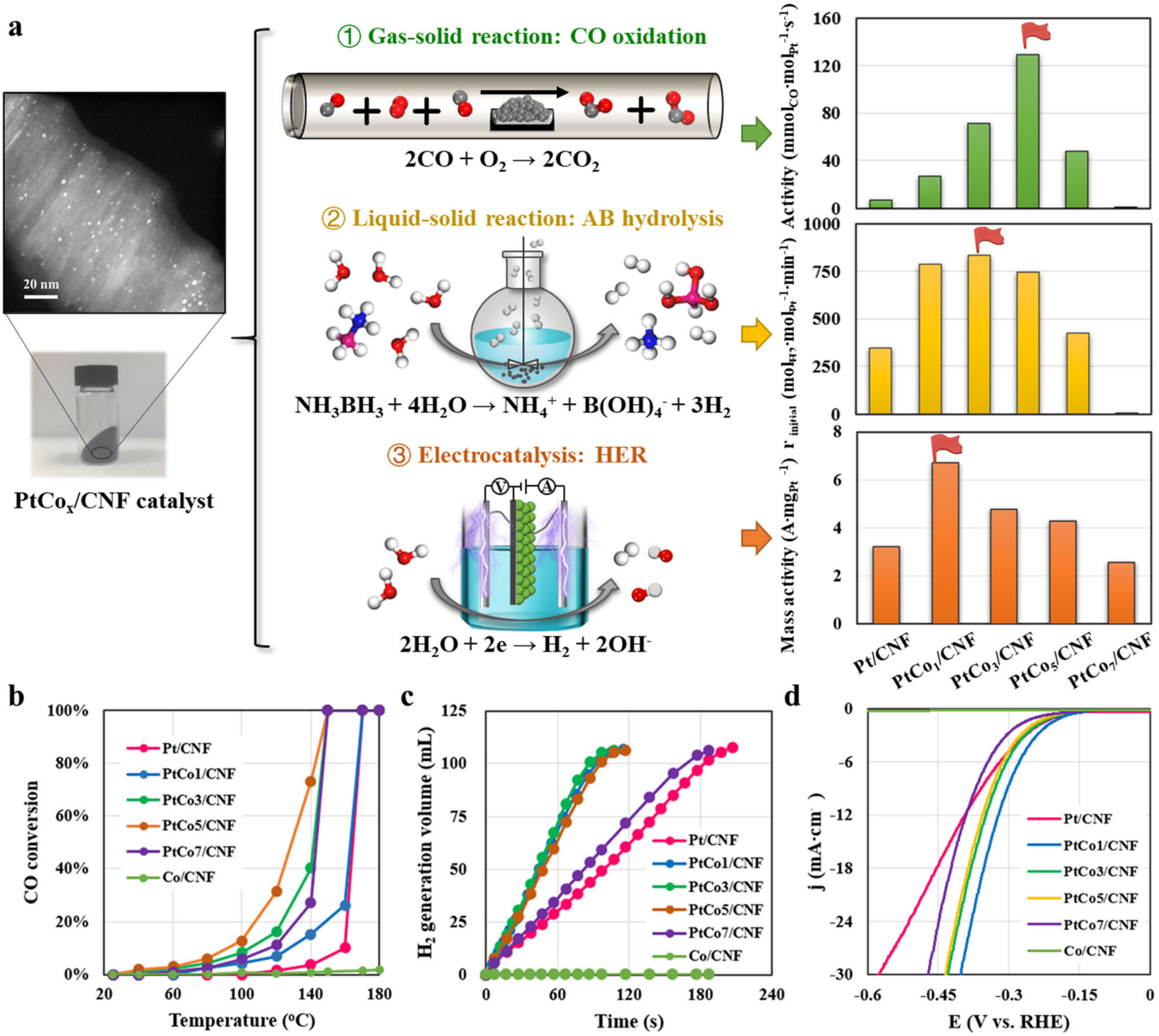

Fig. 1 | Composition- and size-dependent volcano curves. **a** The composition- and size-dependent volcano curves of Pt/CNF and PtCo$_x$/CNF catalysts for CO oxidation, ammonia borane hydrolysis, and HER. **b**–**d** CO conversion as a function of reaction temperature (**b**), hydrogen generation volume as a function of reaction time (**c**), and LSV polarization curves (**d**) for Pt/CNF, PtCo$_x$/CNF, and Co/CNF catalysts.

significantly among the catalysts in Fig. 2b. Monometallic Pt/CNF and Co/CNF exhibit only one reduction peak at 104 °C and 334 °C, respectively. In comparison, the reduction of bimetallic PtCo$_x$/CNF catalysts splits into three new reduction peaks between that of Pt/CNF and Co/CNF, which become intensive with the addition of Co. This indicates the presence of three kinds of Co species based on their interactions with Pt, in which Co in a closer proximity to Pt is likely reduced by the spillover hydrogen at a lower temperature.

The XPS Pt 4*f* spectra depicted in Fig. 2c show the prevalence of metallic Pt^0 species within nanoparticles, whose binding energy possesses a trend of initially increasing and then decreasing, reaching its maximum for PtCo$_1$/CNF with Pt^0 $4f_{7/2}$ and Pt^0 $4f_{5/2}$ at 72.10 and 75.27 eV, respectively. Considering the high electron-conductivity of CNF and the identical Pt loading, the observed binding energy shift mainly arises from the electron transfer between Pt and Co species, whose direction reverses from Pt→Co to Co→Pt with the addition of Co. This observation is very interesting as the electron transfer in either direction, Pt→Co[30,31] or Co→Pt[32,33], has been suggested for Pt–Co alloys in numerous literatures without a consensus. To resolve this debate, the XPS Co 2*p* spectra in Fig. 2d were further deconvoluted and analyzed. The signal-to-noise ratio of Co 2*p* spectra is much lower than Pt 4*f* spectra, particularly for PtCo$_1$/CNF, ascribed to its lower Co loading and smaller Co 2*p* sensitivity factor. In contrast, the other three catalysts exhibit the prevalence of oxidized Co^{m+} species instead of metallic Co^{0+} species with similar Co 2*p* signal strengths. Combining Pt 4*f* spectra in Fig. 2c, it indicates the electron transfer from oxidized Co to metallic Pt species for these catalysts.

To confirm the electron transfer mentioned, theoretical calculations were performed on three different 13-atom Pt–Co bimetallic clusters: $Pt_{10}Co_3$, Pt_7Co_6, and Pt_2Co_{11}. Following geometry optimization and total energy calculations, we selected the low-energy configurations for Bader charge analysis, as illustrated in Fig. 2e. Under similar sizes and regardless of the cluster composition, Pt is found to gain electrons while Co loses electrons, with a total electron transfer of 1.68, 2.59, and 1.32 electrons, respectively. This observation appears to contradict the XPS results, which indicate electron transfer from Pt to Co. However, it is important to note that the Bader charge refers to the total number of electrons, rather than the number of valence electrons (5*d* electron for Pt, and 3*d* electron for Co). Focusing on the Pt 5*d* band in terms of the projected density of state (PDOS) as shown in Fig. 2f,

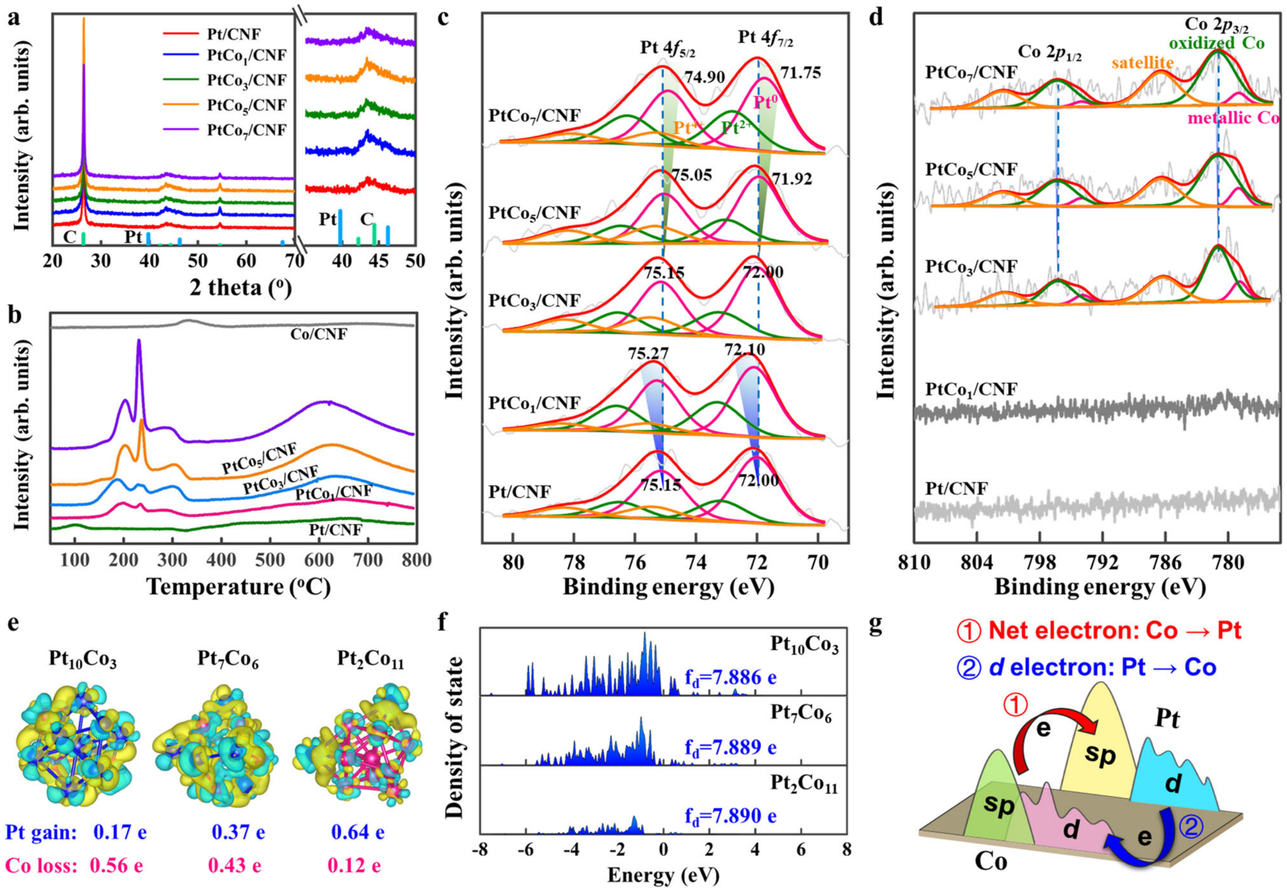

Fig. 2 | Structural characterization of Pt–Co bimetallic catalysts. a–d XRD patterns (**a**), H_2-TPR profiles (**b**), XPS Pt 4*f* spectra (**c**), XPS Co 2*p* spectra (**d**) for Pt/CNF and $PtCo_x$/CNF catalysts. XRD and XPS measurements were conducted on the fresh catalysts. H_2-TPR measurement was performed on the unreduced catalyst precursors. **e**,**f** The differential electron density isosurfaces (**e**) and corresponding PDOS analysis of Pt 5*d* states (**f**) for $Pt_{10}Co_3$, Pt_7Co_6, and Pt_2Co_{11}. **g** The scheme of net electron and *d* electron transfer between Pt and Co within Pt–Co alloy.

number of 5*d* electron by integrating up to the Fermi level is 7.886, 7.889, and 7.890 e, respectively. Similarly, based on the PDOS of the Co 3*d* band in Supplementary Fig. S12, the number of 3*d* electron is calculated as 7.132, 7.252, and 7.279 e, respectively. Hence, the previous debate on electron transfer within Pt–Co alloy can be reasonably addressed by *d* electron transfer from Pt to Co along with net electron transfer from Co to Pt as schematically shown in Fig. 2g. Moreover, the corresponding *d*-band center of Pt has been calculated as −1.62, −1.82, −1.94 and −2.12 eV for Pt_{13}, $Pt_{10}Co_3$, Pt_7Co_6, and Pt_2Co_{11}, respectively. Obviously, the electrons coupling between Pt and Co in the *d* orbitals significantly lowers Pt *d*-band center, which will be further discussed below. Based on the above, the first reduction peak (~200 °C) in H_2-TPR profiles (Fig. 2b) can be reasonably attributed to the reduction of metal precursors to generate Pt–Co alloy, which is dominant for the $PtCo_1$/CNF and $PtCo_3$/CNF catalysts with a higher Pt 4*f* binding energy due to *d* electron transfer from Pt to Co. The further addition of Co leads to the dominance of the second reduction peak (~230 °C) ascribed to the reduction of oxidized Co species by spillover hydrogen from Pt–Co alloy, particularly for $PtCo_7$/CNF, which has the lowest Pt 4*f* binding energy due to electron transfer from oxidized Co to Pt. Additionally, the third reduction peak (~300 °C) could be due to some Co species that are relatively far from Pt–Co alloy and difficult to be reduced.

Support-induced restructuring

Indeed, it is widely known that Co exhibits complete miscibility within Pt across the entire solid solution range, resulting in the formation of alloy. Herein, regarding the three possible types of Co-containing species, aberration-corrected (AC) HAADF-STEM and XAS were employed to gain more insights into these surface sites. The atomic structure of $PtCo_1$/CNF as shown in Fig. 3a exhibits the surface distribution of metal nanoparticles of 1–2 nm, along with some clusters and single atoms around them. The high-resolution image, together with the corresponding fast Fourier transform in Fig. 3b, reveals the lattice fringe with an interplanar spacing of 2.16 Å, which is much smaller than that of pure cubic Pt. This is likely ascribed to the (111) plane of Pt–Co alloy, and confirmed by the EDS line-scanning result. However, the molar ratio of Pt and Co (n_{Pt}:n_{Co}) based on the EDS measurements of more than 40 nanoparticles is statistically determined to be 2:1 (Fig. 3c) rather than the stoichiometric ratio of 1:1. This discrepancy, along with the 3D atom-overlapping Gaussian-function fitting mapping (Fig. 3c), suggests that the less bright, single atoms detached from the nanoparticles are likely isolated Co species.

As indicated by the enhancement of the third reduction peak in H_2-TPR profiles, the AC-HAADF-STEM analysis of $PtCo_3$/CNF in Fig. 3d reveals the presence of more isolated Co species surrounding the metal nanoparticles. Moreover, it can be seen some species with low contrast adheres to these nanoparticles. The high-resolution image of Fig. 3e exhibits the truncated cuboctahedron morphology of the metal particles, which is known to minimize its surface energy. The outer surfaces of metal nanoparticles exhibit coverage by Co-containing species, as elucidated by the EDS line-scan analysis depicted in Fig. 3f. The above results are in line with the high oxytropism of Co, and confirmed by the selected particles in other areas as shown in Supplementary Figs. S13 and S14. Further addition of Co promotes the formation of surface CoO_x species and phase segregation to generate the adjacent Co_3O_4 clusters, as evidenced by the interplanar spacing in

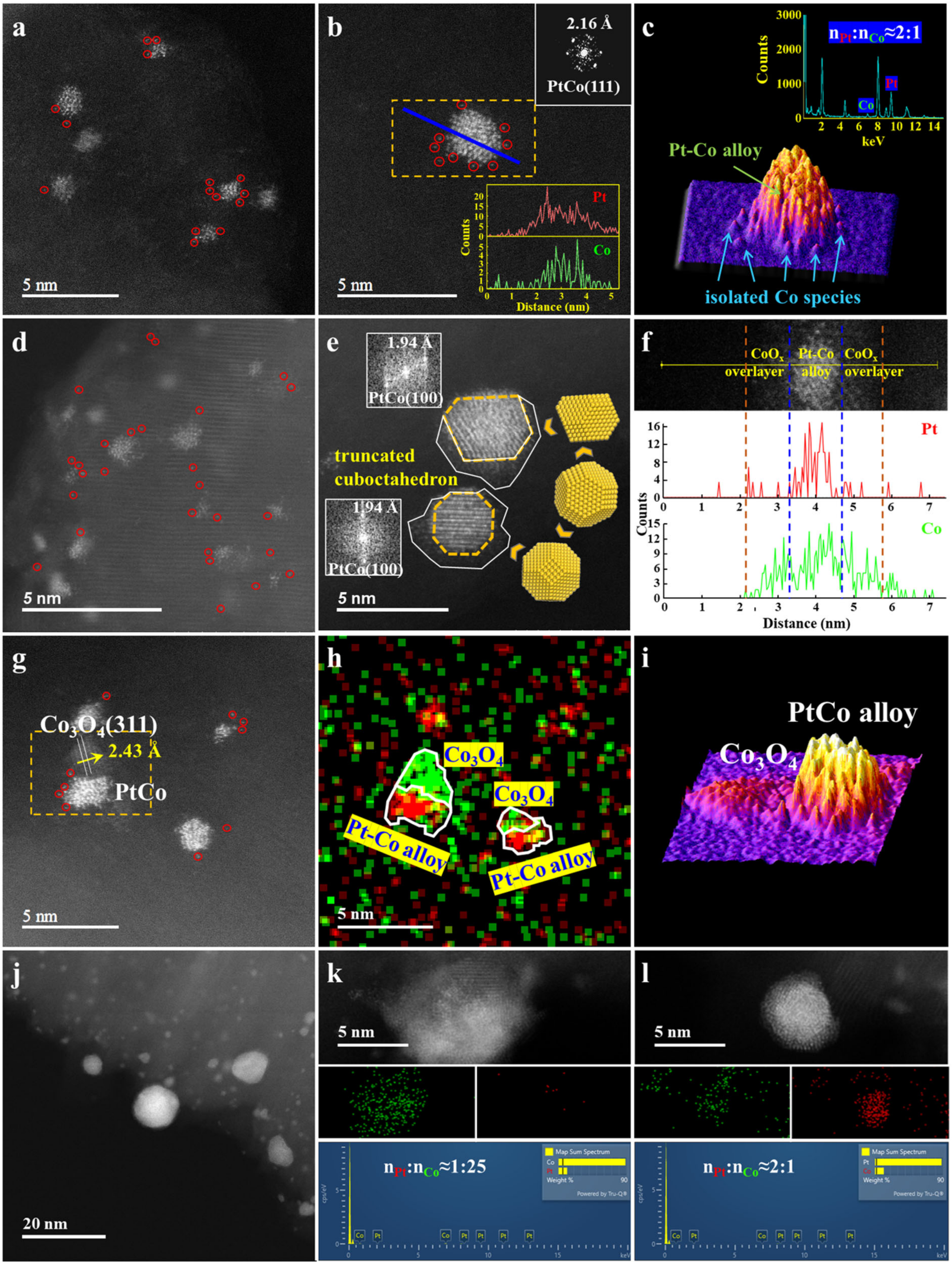

Fig. 3 | Microscopy characterization and analysis. **a**–**c** AC-HAADF-STEM image (**a**), high-resolution image and corresponding fast Fourier transform as well as EDS line-scanning results (**b**), and 3D atom-overlapping Gaussian-function fitting mapping as well as n_{Pt}:n_{Co} determined by EDS (**c**) for the fresh $PtCo_1$/CNF catalyst. **d**–**f**, AC-HAADF-STEM image (**d**), high-resolution image and corresponding projections of truncated cuboctahedron model (**e**), and EDS line-scanning results (**f**) for the fresh $PtCo_3$/CNF catalyst. **g**–**i**, AC-HAADF-STEM image (**g**), EDS mapping result (**h**), and 3D atom-overlapping Gaussian-function fitting mapping (**i**) for the fresh $PtCo_5$/CNF catalyst. **j**–**l**, AC-HAADF-STEM image (**j**), EDS mapping results of Co-rich alloy (**k**) and Pt-rich alloy (**l**) for the fresh $PtCo_7$/CNF catalyst.

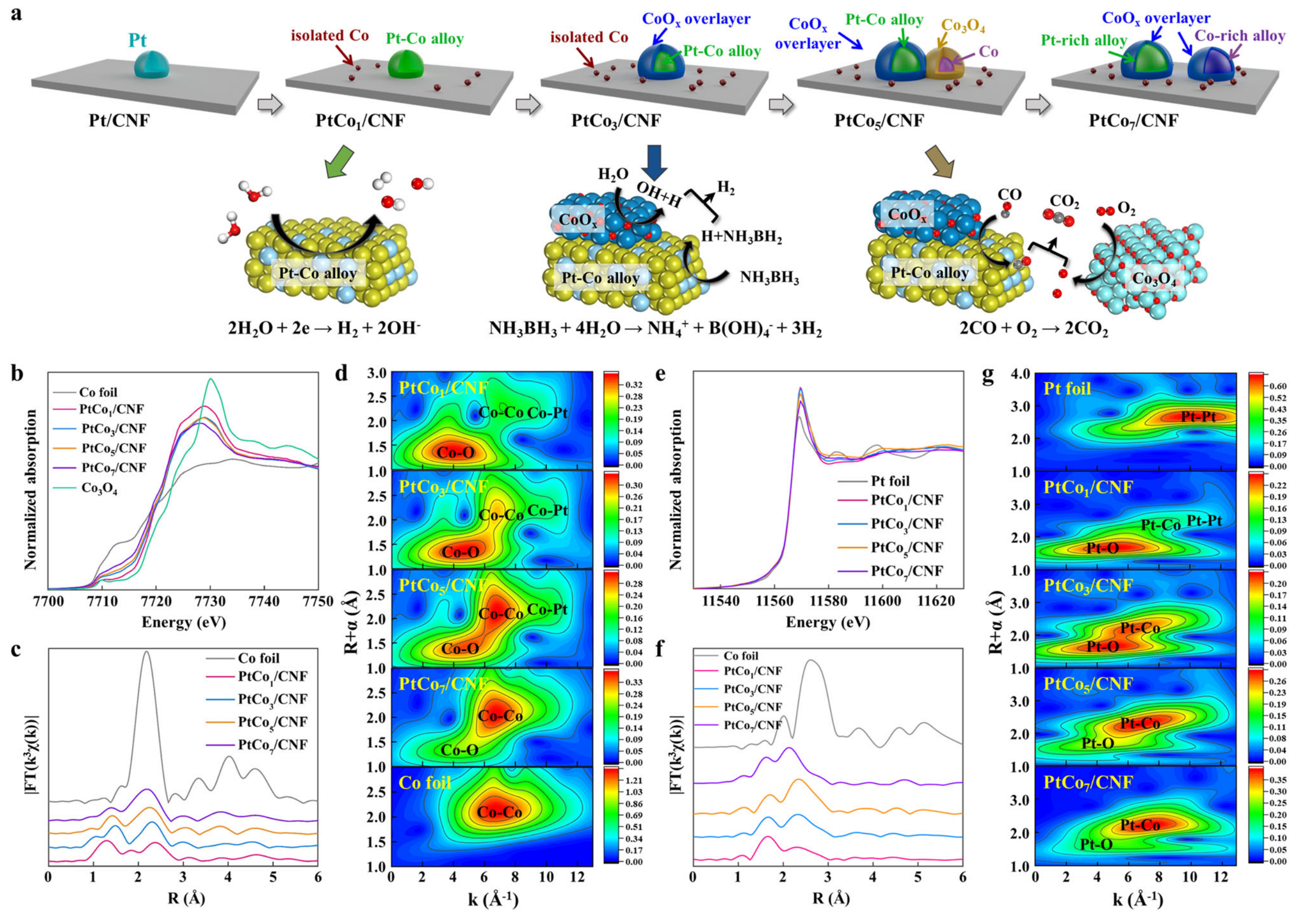

Fig. 4 | Support-induced restructuring of Pt–Co bimetallic catalysts. a Scheme of support-induced restructuring of bimetallic PtCo$_x$/CNF catalyst for CO oxidation, ammonia borane hydrolysis, and hydrogen evolution reaction. The white, gray, red, yellow, and blue spheres represent the H, C, O, Pt, and Co atoms, respectively. **b**–**d** Normalized Co *K*-edge XANES spectra (**b**), FT Co *K*-edge k^3-weighted FT-EXAFS spectra (**c**), and the corresponding WT-EXAFS of the Co *K*-edge signal (**d**) of the fresh PtCo$_x$/CNF catalysts. **e**–**g**\ Normalized Pt L_{III}-edge XANES spectra (**e**), FT Pt L_{III}-edge k^3-weighted FT-EXAFS spectra (**f**), and the corresponding WT-EXAFS of the Pt L_{III}-edge signal (**g**) of the fresh PtCo$_x$/CNF catalysts.

Fig. 3g for PtCo$_5$/CNF. These observations are verified by EDS mapping results (Fig. 3h), the fitting mapping (Fig. 3i), and those in other areas (Supplementary Fig. S15). These findings also support the second reduction peak in H$_2$-TPR profile ascribed to the formation of Co$_3$O$_4$, as intensified for PtCo$_5$/CNF.

In the case of PtCo$_7$/CNF, which possesses the highest Co content, while the majority of the metal particles are maintained at 2–3 nm, discernible agglomerations of metal particles are observed on the catalyst surface, as illustrated in Fig. 3j. EDS mapping results reveal that these agglomerations consist of either Co-rich alloys (Fig. 3k, Supplementary Figs. S16 and S17) or Pt-rich alloys (Fig. 3l, Supplementary Figs. S18 and S19). This suggests that the large agglomerations undergo structural collapses, culminating in phase segregation into the concomitant amorphous Co-rich and Pt-rich alloys. Typically, when CNF serve as a support, the binding energy of its exposed surface sites to the doped Pt atoms exhibited a range from −2.03 eV on the basal plane to −11.01 eV on the edge plane[34]. Thus, it is reasonable to deduce that the platelet CNF with the maximum edge-to-basal surface area should form strong Pt–C bonding, triggering the observed atoms detachment, segregation, and even particle collapse. Furthermore, from a thermodynamic standpoint, the observations are consistent with the established phase stability, which favors phase separation towards the Pt–Co phase with lower Co content existing in a mixture of two or more Pt–Co phases[35–37]. Accordingly, the possible restructuring process of Pt–Co bimetallic catalyst by continuously adding Co can be schematically depicted in Fig. 4a.

Figure 4b shows the normalized Co *K*-edge XANES spectra. The pre-edge peak positions of these bimetallic catalysts are quite close to that of Co$_3$O$_4$, indicating a majority of Co exists as oxidized species over CNF surfaces as characterized by XPS Co 2*p* spectra in Fig. 2d. Moreover, the addition of Co causes the pre-edge peak to shift towards that of Co foil as an indication of decreased valence state. This observation is consistent with the microstructure of Pt-rich alloy along with numerous surrounding isolated Co species for PtCo$_1$/CNF. Typically, these isolated Co species strongly interact with CNF via Co–O bond with a high valence state, and their percentage decreases with the addition of Co, leading to a decrease in the average valence state of Co. Figures 4c, d show FT Co *K*-edge k^3-weighted EXAFS spectra and the corresponding WT-EXAFS of the Co *K*-edge signal, respectively, and the corresponding fitting results are summarized in Supplementary Table S1. Clearly, the coordination number of Co–O decreases with the addition of Co, while that of Co-Co increases. The trend of the coordination number agrees with the formation of Co-rich alloy as shown in Fig. 4a.

Figure 4e displays the normalized Pt L_{III}-edge XANES spectra, whose white-line (WL) intensity decreases upon Co addition. Regarding the well-studied relation between WL intensity and the electron occupancy of Pt 5*d* band, this further confirms the above Pt 4*f* XPS results (Fig. 2c) of *d* electron transfer from metallic Pt to metallic Co, which reverses from oxidized Co to metallic Pt. Figure 4f, g show FT Pt L_{III}-edge k^3-weighted EXAFS spectra and the corresponding WT-EXAFS of the Pt L_{III}-edge signal, respectively, and the corresponding fitting

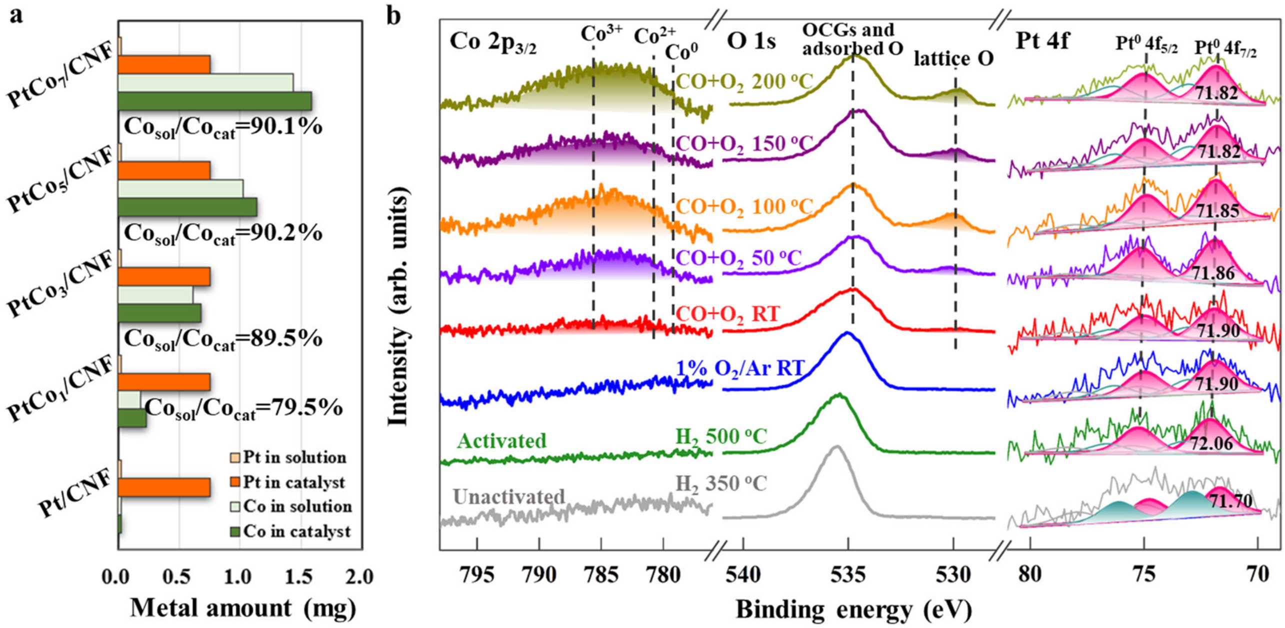

Fig. 5 | Restructuring of Pt–Co bimetallic catalysts under varying reaction conditions. **a** Comparison of the amount of metal in the fresh catalyst and acid solution by acid leaching. **b** Quasi in situ XPS spectra of Co $2p_{3/2}$, O 1*s* and Pt 4*f* region for the precursor of $PtCo_5$/CNF catalyst under reduced and oxidized atmosphere.

results are summarized in Supplementary Table S2. Clearly, the coordination number of Pt–O decreases with the addition of Co, while that of Pt–Co increases. This also supports the formation of Co-rich alloy, which involves highly dispersed Pt species coordinated with Co, and prevents Pt from forming Pt–O bond with adsorbed oxygen. To this point, it is found that the support-induced restructuring of Pt–Co bimetallic catalysts is mainly driven by the strong Pt–C bonding within the metal-support interfaces as depicted in Fig. 4a. Initially, Co alloys with Pt to form Pt-rich alloys along with surrounding isolated Co species (n_{Pt}:n_{Co} = 1:1). Then, Co segregates to the outer surface to form an epitaxial CoO_x overlayer (n_{Pt}:n_{Co} = 1:3), followed by its detachment and generation of adjacent Co_3O_4 clusters (n_{Pt}:n_{Co} = 1:5). Finally, the phases of bimetallic particles collapse and segregate into the concomitant amorphous Co-rich and Pt-rich alloys (n_{Pt}:n_{Co} = 1:7).

Surface adsorbate-induced restructuring

We further investigated these interfacial sites under varying reaction conditions. Acid leaching was firstly carried out for these catalysts, and the amount of metal in the acid solution was determined by ICP and compared with that in the fresh catalyst in Fig. 5a. It can be seen that Pt remains highly stable over CNF surface with negligible dissolution in acid, while Co tends to be easily dissolved. However, the amount of Co dissolution for $PtCo_1$/CNF is lower than that for the other three catalysts. Regarding the highest percentage of Pt–Co alloy for $PtCo_1$/CNF, it suggests that the oxidized Co species including surface isolated Co–O, CoO_x overlayer, and Co_3O_4 are easily dissolved in acid, while the metallic Co within Pt–Co alloy is relatively stable and resistant to acid leaching due to its strong interaction with Pt. The similar treatments under alkaline and neutral conditions were also conducted, where the dissolved amounts of Pt and Co were below the detection limit. Moreover, exemplifying with the most active catalyst, the used $PtCo_1$/CNF catalyst shows negligible agglomeration of metal particles for HER under alkaline conditions (Supplementary Fig. S20), with particle sizes determined to be 1.4 nm. This finding aligns with the robust metal-support interaction, attributed to the elevated edge-to-basal surface area ratio of CNF, which effectively precludes metal particle agglomeration. A comparable phenomenon is observed in the $PtCo_3$/CNF catalyst when subjected to nearly neutral conditions for the hydrolysis of ammonia borane, as illustrated in Supplementary Fig. S21. Furthermore, the structural characteristics of the PtCo/CNF catalyst during the electrocatalytic process were elucidated through in situ Raman and XRD analyzes. The XRD patterns, as depicted in Supplementary Fig. S22, demonstrate that the primary diffraction peaks, associated with the carbon support, remain essentially invariant throughout the range of applied voltages. This finding implies a lack of substantial alterations in the carbon interlayer spacing, corroborated by the almost identical I_D/I_G ratios observed in the Raman spectra (Supplementary Fig. S23). Moreover, the absence of new peaks ascribed to metal oxides suggests the high stability. Hence, the negative effects of metal leaching and particle agglomeration, as the causes for active sites loss, on HER and ammonia borane hydrolysis can be minimal.

For CO oxidation, we took the example of the most active $PtCo_5$/CNF catalyst for studying its stability under reaction conditions. Quasi in situ XPS measurements were performed to probe the structural changes under reduced (H_2 for catalyst reduction) and oxidized (CO and O_2 for catalytic reaction) atmosphere, and the results are shown in Fig. 5b. Under reduced atmosphere, increasing the temperature facilitates the reduction of non-metallic precursors to metallic Pt species, which exhibit the highest binding energy by transferring *d* electron to Co species. After cooled down to room temperature and passivated by 1% O_2/Ar, there is a significant decrease in Pt 4*f* binding energy as an indication of electron gain from the generated CoO_x overlayer. In contrast, there were negligible signals in the Co $2p_{3/2}$ region, which is also observed in Fig. 2d for $PtCo_1$/CNF involving Pt–Co alloy and isolated Co species. Accordingly, it is very likely that under the reduced atmosphere, both Pt and Co mainly exist as metallic state in the form of Pt–Co alloy, along with some isolated Co species. Interestingly, the Co 2*p* signal appears after switching to the oxidized atmosphere, and is dominated by the oxidized Co^{3+} and Co^{2+} species. This agrees with the segregation of Co from Pt–Co alloy to the formation of CoO_x overlayer and further adjacent Co_3O_4 nanoparticles, which are promoted by rising the reaction temperature regarding the strong Co–O bonding. Correspondingly, the signal ascribed to lattice oxygen in Co_3O_4 nanoparticles also appears and becomes intensified in the O 1*s* region. In the Pt 4*f* region, the binding energy exhibits a decreased trend by rising temperature, ascribed to the segregation of Co from Pt–Co alloy and the simultaneous oxidation, which reverses the electron transfer.

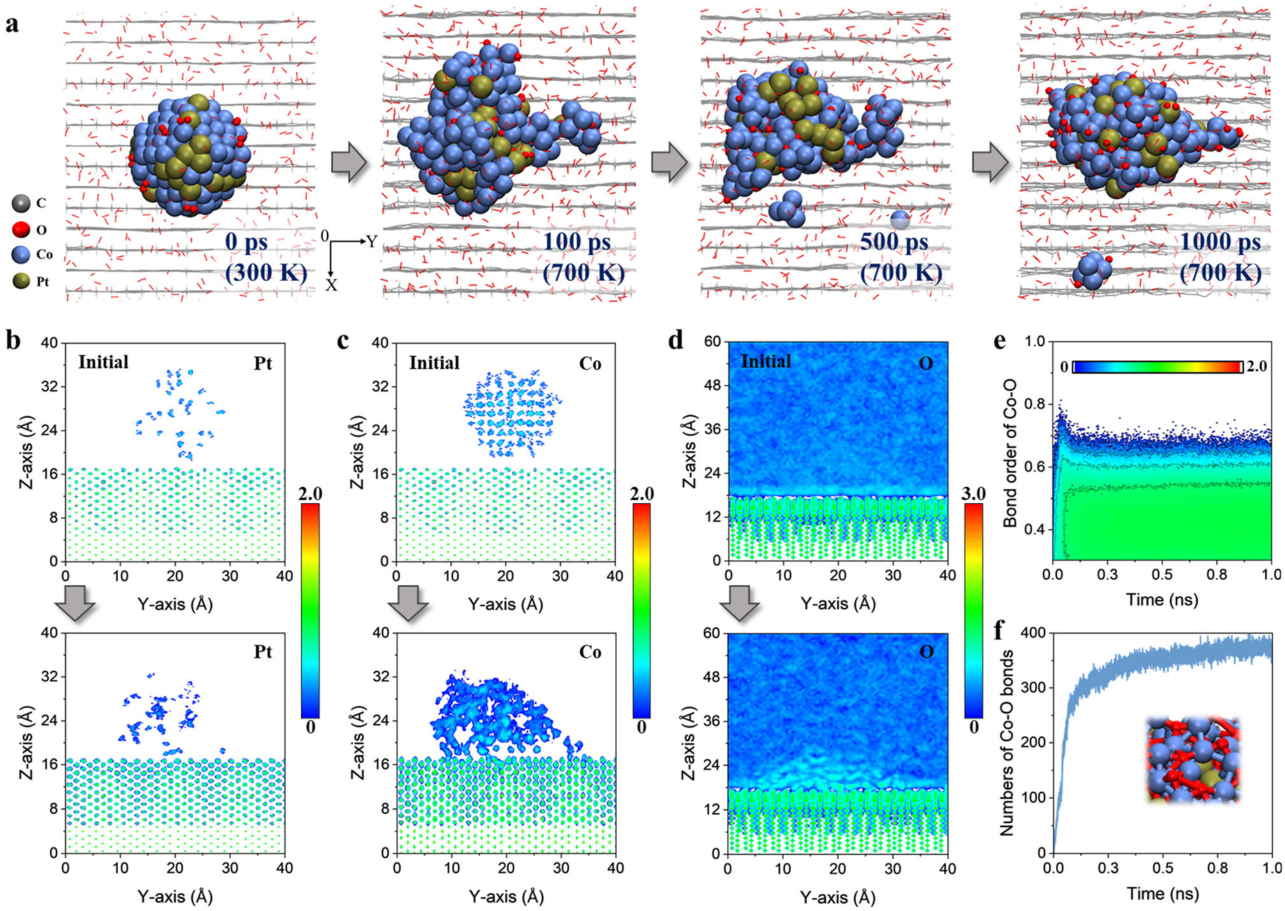

Fig. 6 | Simulated restructuring of Pt–Co bimetallic catalyst. a Snapshot of the restructuring behavior of the $PtCo_5$ catalyst under oxidized atmosphere. **b**–**d** Contour plots of concentration gradient of Pt (**b**), Co (**c**), and O (**d**) elements at the initial and final stages of the simulation. **e** The gradient distribution of Co–O bond order as a function of the simulation time. **f** The number of Co–O bond as a function of the simulation time.

Moreover, Pt remains stable in a metallic state within the Pt–Co alloy and resists oxidation under 150 °C. Such trend was further verified by the measurement of near-ambient-pressure XPS (NAP-XPS) as shown in Supplementary Fig. S24. In contrast, the monometallic Pt/CNF catalyst, as depicted in Supplementary Fig. S25, demonstrates that both the binding energy and the relative abundance of Pt species remain nearly constant up to 150 °C; however, upon further temperature elevation, a partial oxidation of Pt is observed.

Classical molecular dynamics (CMD) simulations were conducted to gain a deeper understanding of the above restructuring, and a dynamic view of the mechanism is shown in Supplementary Movie S1. As illustrated in Fig. 6a, the $PtCo_5$ nanoparticle, at the outset of the energy relaxation phase (0 ps), retains a stable face-centered cubic (FCC) truncated octahedral structure consisting of 201 atoms (34 Pt and 167 Co). The homogeneous distribution of Pt and Co atoms within the nanoparticles is clearly demonstrated in Fig. 6b, c, respectively. Upon introducing oxygen, the $PtCo_5$ nanoparticle experiences a significant deformation, transitioning into an amorphous form due to its strong interaction with CNF. Simultaneously, Co species move to the surface, forming a proximal oxidized cobalt cluster (100 ps). Prolonging the simulation duration to 500 ps reveals the emergence of a Co4 cluster and individual Co atoms detaching from the bimetallic nanoparticle onto the support CNF surface, culminating in oxidation by the end of the simulation (1000 ps). Correspondingly, the surface Pt atoms migrate inward and enriches the interior nanoparticles in Fig. 6b. Furthermore, oxygen species, enriched on the CNF surface at the initial stage, migrate and form a volcano-like overlay above the nanoparticle, as shown in Fig. 6d, indicative of epitaxial CoO_x overlayers and consistent with experimental observations. These migration behaviors are verified by the calculated radial density function of Pt and Co atoms in relative to the particle mass center as depicted in Supplementary Fig. S26.

The bond strengths of Co–O-bonds, primarily about 0.5 as shown in Fig. 6e, show that oxygen forms strong ionic bonds with Co, and a small part of the bond level is between 0.6-0.8, ascribed to the migration of oxygen within nanoparticle to form a stronger Co–O bonding. Consequently, the initial sharp increase in Co–O bond numbers, seen in Fig. 6f, suggests that solute oxygen diffuse to Co–Pt interfaces via an interexchange mechanism[38]. Once oxygen reaches the interfaces, the stronger Co–O bond in comparison with Pt–O bond favors Co segregation. Given that the outward diffusion coefficients of Co exceed the inward diffusion of oxygen into the nanoparticle, Co forms an oxidized overlayer on the particle surface, and thus the strong Co–O bonding serve as the driving force behind the adsorbate-induced restructuring. Such migration trends were further confirmed by aberration-corrected environmental scanning transmission electron microscope dark field (ESTEM-DF) analysis in Supplementary Fig. S27. The transition from a reduced to an oxidized environment induces Co segregation to the outer surface of bimetallic nanoparticle, leading to the formation of oxidized CoOx overlayers, with some detached Co species undergoing nucleation and growth onto the CNF surface.

Synergy-dependent volcano curves

Upon disclosing the important role of the strong Pt–C and Co–O bondings behind the support- and adsorbate-induced restructuring, SSITKA was conducted to correlate them with catalytic performance. As shown in Supplementary Fig. S28, $PtCo_5$/CNF exhibits a small amount of $^{16}O^{18}O$ via the isotopic switch from $C^{16}O + {}^{16}O_2 + Ar$ to $C^{16}O + {}^{18}O_2 + Ar$ under steady state. The observed $^{16}O^{18}O$ is stable after reaching the maximum, indicating that it originates from the impurity in the feed gas $^{18}O_2$. Furthermore, not only $C^{16}O^{18}O$ but also $C^{18}O_2$ can be detected in the products, ascribed to the isotopic exchange within the reaction intermediate (from $^{18}O^*\text{-}{}^{18}O\text{-}C^*\text{-}{}^{16}O$ to $^{16}O^*\text{-}{}^{18}O\text{-}C^*\text{-}{}^{18}O$) via CO-assisted rather than direct O_2 dissociation. Because the reaction between $C^{16}O$ and lattice $^{16}O/^{18}O$ only yields $C^{16}O_2/C^{16}O^{18}O$, the detection of $C^{18}O_2$ in products suggests another pathway of CO-assisted O_2 dissociation ($CO + O_2 \rightarrow OCOO \rightarrow CO_2 + O$) as a competitor of the lattice oxygen pathway (CO + lattice O → CO_2). TKA was further conducted to evaluate the competition between these two pathways. It can be seen in Supplementary Fig. S29 that, after switching from Ar to $C^{16}O + {}^{18}O_2 + Ar$, the bimetallic $PtCo_x$/CNF catalysts demonstrate a step of first increase then decrease in the signal of $C^{16}O_2$, which is absent for the monometallic Pt/CNF catalyst. Accordingly, this step is likely ascribed to the reaction between $C^{16}O$ and lattice ^{16}O within Co oxides. $PtCo_5$/CNF with the highest intensity of this step could involve the largest amount of lattice oxygen, thus providing the highest reaction rate for the lattice oxygen pathway. Moreover, the similar intensity of $C^{18}O_2$ for these bimetallic catalysts indicates the similar reaction rates for the CO-assisted O_2 dissociation pathway. Therefore, the abundant Co_3O_4 nanoparticles over $PtCo_5$/CNF surface provide more lattice oxygens to the adjacent Pt–Co alloys for the adsorbed CO oxidation, which significantly promotes the lattice oxygen redox pathway.

Hence, for CO oxidation as shown in Fig. 4a, the highest CO conversion was achieved by $PtCo_5$/CNF, which has the site structure of Pt–Co alloy along with adjacent Co_3O_4 clusters. This is because the transfer of *d* electrons from Pt to Co can decrease the electron occupancy of Pt 5*d* band, resulting in lower CO site coverage to promote its association with oxygen. More importantly, the adjacent Co_3O_4 nanoparticles provide abundant lattice oxygen species that can transfer to Pt–Co alloy to react with CO. Such promotional effect has been also demonstrated by Song et al., where the participation of lattice oxygen from CoO at the formed Pt–CoO interfaces significantly enhances CO oxidation[39]. Such synergy offers an almost 20-fold increase in catalytic activity for CO oxidation in comparison with monometallic Pt. For ammonia borane hydrolysis, the highest hydrogen generation rate was achieved by $PtCo_3$/CNF, which has the site structure of Pt–Co alloy with an epitaxial CoO_x overlayer (1–2 atomic layers). Generally, water dissociation is considered as the key step for monometallic Pt catalyst, regarding its strong ability to activate ammonia borane[40]. In contrast, water dissociation can occur more easily on metal oxides, particularly on amorphous metal oxides with abundant surface defects[41]. Therefore, the Pt–Co alloy and epitaxial CoO_x overlayer act as the active sites for the activation of ammonia borane and water, respectively, significantly promoting hydrogen generation. For HER, the highest catalytic performance was achieved by $PtCo_1$/CNF in the form of Pt–Co alloy. This can be ascribed to the enhanced coupling of electrons between Pt and Co in the *d* orbitals to afford a lower Pt *d*-band center as discussed above, which can remarkably minimize the Pt-H bond energy and reduce the Gibbs free energy of H adsorption to promote the HER kinetics[42,43]. Hence, a quantitative comparison of synergy among different interfacial sites can be further made in Supplementary Figs. S30-S32 based on the estimation of their dispersions as shown in Supplementary Note. Further incorporating the above mesokinetics information, the resultant synergy-dependent volcano curves as depicted in Fig. 7 represents an advancement of traditional composition-/size-dependent volcano curves in Supplementary Figs. S6, S7, and S11, which enable the microscopic-to-macroscopic transition to rationalize the Pt–Co bimetallic catalyst design for the three reactions[12]. Moreover, the synergy-dependent volcano curves gained from this work can inform the development of computational models and machine learning algorithms that may, in the future, provide even more accurate a-priori predictions of catalyst performance.

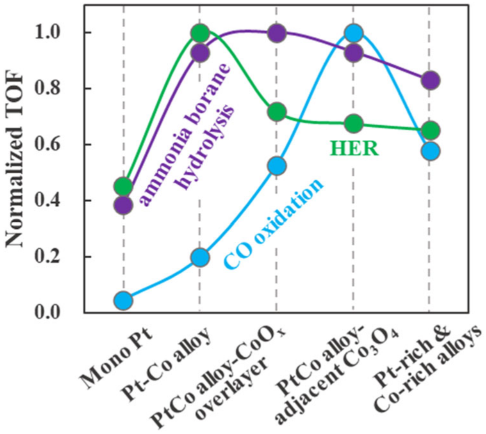

Fig. 7 | Synergy-dependent volcano curves. The synergy-dependent volcano curves of bimetallic platinum-cobalt catalysts for CO oxidation, ammonia borane hydrolysis, and hydrogen evolution reaction.

Discussion

In conclusion, we present a proof-of-concept study by revealing both the support- and adsorbate-induced restructuring of Pt–Co bimetallic catalysts, and the related interplays among different interfacial sites to propose the synergy-dependent volcano curves. Exemplified by three representative yet disputed reactions, namely CO oxidation (gas-phase), ammonia borane hydrolysis (liquid-phase), and hydrogen evolution reaction (electrocatalysis), a series of CNF-supported Pt–Co bimetallic catalysts were prepared, whose catalytic performances can be similarly correlated with either the catalyst composition or particle size by volcano curves as previous studies. Microscopic and spectroscopic characterization, theoretical calculation, isotopic labeling, and SSITKA were employed to unveil the atomic restructuring induced by support and adsorbate. Driven by the strong Pt–C bonding within the metal-support interfaces and Co–O bonding within the metal-adsorbate interfaces, the introduction of Co into Pt catalysts initiates the formation of Pt-rich alloys alongside isolated Co species. Subsequently, Co segregates to the outer surface of the Pt–Co alloy, forming an epitaxial CoO_x overlayer. This is followed by migration and the formation of adjacent Co_3O_4 clusters. Ultimately, the bimetallic particles undergo phase collapse into concomitant amorphous Co-rich and Pt-rich alloys.

Upon investigation of active site stability and related reaction mechanism, the interplays among different interfacial sites have been disentangled. For CO oxidation, Pt–Co alloy along with adjacent Co_3O_4 clusters can not only remove *d* electrons from Pt to lower CO site coverage but also provide abundant lattice oxygen species. Such synergy is promoted under reaction conditions, which facilitates the lattice oxygen-promoted pathway rather than the CO-assisted O_2 dissociation pathway to significantly enhance CO conversion. For ammonia borane hydrolysis, Pt–Co alloy along with an epitaxial CoO_x overlayer acts as the active site for the activation of ammonia borane and water, respectively. Such synergy lowers the activation energy to significantly promote hydrogen generation. For HER, the exposed Pt–Co alloy can avoid the detrimental steric effects of CoO_x overlayers or adjacent Co_3O_4 clusters, and its internal electron coupling in the *d* orbitals affords a lower Pt *d*-band center. Such synergy minimizes the Pt-H bond energy to reduce H adsorption and promotes hydrogen evolution. As a result, three distinct synergies, involving lattice oxygen redox from Pt–Co alloy/Co_3O_4 clusters, dual-active sites engineering via Pt-rich alloy/CoO_x overlayer, and electron coupling within exposed alloy, were identified and quantified to establish the synergy-dependent volcano curves. The introduction of these synergy-dependent volcano curves marks a significant advancement over traditional composition- or size-dependent ones, offering improved methods for benchmarking and designing highly efficient Pt-based bimetallic catalysts.

Methods

Catalyst preparation

Carbon nanofibers (CNF) were employed as catalyst support and prepared by catalytic chemical vapor deposition (CCVD) according to the following steps: a certain amount of Fe_3O_4 catalyst was preloaded in a tubular furnace and heated to 600 °C at a ramp rate of 5 °C·min^{-1} under a flow of H_2/Ar mixture (25/75 mL·min^{-1}). After 3 h reduction, the inlet gas was switched to CO/H_2 (80/20 mL·min^{-1}) for CNF growth, which was maintained at the same conditions for another 24 h. After cooling down to room temperature under Ar, the as-prepared CNF was further purified by mixing with a diluted HNO_3 solution (Sinopharm Chemical Reagent Co., Ltd., China) under vigorously stirring for 24 h at 80 °C. The purified CNF was filtered and washed by deionized water for several times, and then dried at 120 °C for 12 h.

The CNF supported monometallic Pt and bimetallic Pt–Co catalysts were prepared by incipient wetness impregnation method. Typically, a certain amount of CNF was mixed with the solution of $H_2PtCl_6 \cdot 6H_2O$ (Sinopharm Chemical Reagent Co., Ltd., China) and $Co(NO_3)_2{\cdot}6H_2O$ (Sinopharm Chemical Reagent Co., Ltd., China). The Pt loading was kept at 0.75 wt% for all the catalysts, while the Co loading was adjusted with the molar ratio of Pt to Co, n_{Pt}:n_{Co}, of 1:1, 1:3, 1:5, and 1:5. The impregnated samples were dried at ambient conditions and then at 80 °C for 12 h each. The as-obtained catalyst precursors were reduced by a continuous flow of pure H_2 (60 mL·min^{-1}) at 500 °C. After 2 h reduction, the as-prepared catalysts were cooling down to room temperature under Ar atmosphere, followed by passivated under a flow of 1% O_2/Ar (60 mL·min^{-1}) for 20 min to prohibit bulk oxidation. As a result, the as-obtained catalysts were denoted as $PtCo_x$/CNF, where x represents the molar ratio of Co to Pt.

Catalyst characterization

In this study, those that do not specifically mention in situ characterization are ex situ characterizations. X-ray diffraction (XRD) characterization was conducted on a Rigaku D/Max 2550VB/PC diffractometer using Cu Kα radiation. High-angle annular dark-field scanning transmission electron microscopy (HAADF-STEM) analysis were carried out on a Tecnai G2 F20 S-Twin instrument. The aberration-corrected high-angle annual dark-field STEM (ACHAADF-STEM) and energy dispersive X-ray (EDS) analyzes were carried out on a Hitachi HF5000 scanning transmission electron microscope with a Cs corrector working at 200 kV. H_2 temperature-programmed reduction (H_2-TPR) measurements were carried out using a Micromeritics AutoChem II 2920 instrument equipped with a TCD-detector. X-ray photoelectron spectroscopy (XPS) was performed on a Kratos XSAM-800 spectrometer using a Mg Kα radiation source. For high-resolution measurements, a monochromatic Al Kα X-ray source (hν = 1486.6 eV) was employed in conjunction with a SPECS PHOIBOS 150 electron energy analyzer, which provided a total energy resolution of 0.50 eV. The binding energy was calibrated using a polycrystalline Ag foil. Quasi in situ XPS spectra were captured using a VG MultiLab 2000 spectrometer, equipped with an Omicron Sphera II hemispherical electron energy analyzer. The system utilized a monochromatic Al Kα X-ray source, operating at an anode voltage of 15 kV and a power of 300 W, which could provide an energy resolution of 0.47 eV. The catalysts were treated under the real reaction conditions with elevated temperature in a homemade reaction chamber under ambient pressure, and then transferred to the XPS analysis chamber for XPS measurement through a load-lock gate without exposure to air. The metal leaching experiments were performed by treating these catalysts in alkaline, neutral, and acidic conditions, respectively. Specifically, 0.50 g catalyst was mixed with 50 mL diluted HNO_3 (0.01 M, Adamas), water, and KOH solution (0.01 M, Adamas) under magnetic stirring for 30 min at room temperature, respectively. The treated catalysts were filtered, washed and dried at 80 °C for 12 h. The contents of Pt and Co in catalyst and acid solution were determined by inductively coupled plasma atomic emission spectrometer (ICP-AES) on a Varian 710-ES apparatus.

X-ray absorption fine structure (XAFS) spectroscopy at the Pt L_{III}-edge and Co K-edge was performed at the BL11B beamline of the Shanghai Synchrotron Radiation Facility (SSRF), which operates at 3.5 GeV with a current of 220 mA. A double-crystal Si(111) monochromator was utilized to provide the monochromatized X-ray beam, achieving an energy resolution of $\Delta E/E \sim 1.4 \times 10^{-4}$. The XAFS spectra were collected in fluorescence mode using an Ar-filled Lytle detector. Before the measurement, the sample was reduced under H_2 at 500 °C for 2 hours, then pressed into a wafer (approximately 20 mg) and sealed with Kapton tape, which was carried out under a post-reduction and atmospheric exposure state. The absorption edge of a pure Pt foil was used to calibrate the X-ray energy. XANES and EXAFS analyzes were conducted using Athena and Artemis, which are implemented in the Demeter program package. The first shell was fitted (magnitude and imaginary parts) in the range R = 1.6–3.0 Å. The energy shift (ΔE_0) was constrained to be the same for all scatterers. Wavelet-transformed k^3-weighted EAXFS was employed using the Hama Fortran code. A Morlet function with $\kappa = 10$, $\sigma = 1$ was used as the mother wavelet to provide an overall distribution. NAP-XPS measurements were carried out at Beamline 20U in Shanghai Synchrotron Radiation Facility (SSRF). In situ XPS spectra were recorded with a Hipp-2 analyzer (ScientaOmicron) using a monochromatic Al Kα radiation source (hν = 1486.6 eV, SPECS). In situ Raman measurements were performed on a Renishaw inVia Qontor Raman Microscope system at room temperature. The electrode potentials were set with reference to HER electrolysis experiments (−0.57, −0.67, −0.77, −0.87, −0.97, −1.07, −1.17, −1.27 V vs. RHE). A Leica 50× long working distance objective lens was employed for precise focusing. The excitation source was a 532 nm laser with an intensity set to 10%. In situ XRD measurements were conducted on a Bruker Db ADVANCE multifunction X-ray diffractometer, with electrode potentials aligned with those of the Raman measurements. Aberration-corrected environmental scanning transmission electron microscope dark field (ESTEM-DF) images were recorded on a Hitachi HF5000 microscope at 200 kV.

Catalytic testing

The catalytic test of CO oxidation was performed in a fixed bed reactor. The catalyst was sieved to the particle size of 0.075-0.106 mm before the reaction. Then, 0.02 g catalyst was preloaded on the quartz wool, which was placed in the center of a U-shaped reactor. The reactant gas composition was 1.0 vol.% CO + 20.0 vol.% O_2 in Ar, and the flow rate of was 20 mL·min^{-1} to reach a gas hourly space velocity of 60,000 ml·$g_{cat}^{-1} \cdot h^{-1}$. The influent and effluent gases were analyzed by an online Agilent 7890 gas chromatograph (GC) equipped with a thermal conductivity detector (TCD).

The catalytic test of ammonia borane hydrolysis was performed in a three-necked flask equipped with a Teflon-coated magnetic stirring bar, which was immersed in a water bath to control the reaction temperature. Prior to the reaction, 0.1 g catalyst was preloaded in the flask, which was connected with a water-filled gas burette. The reaction was started by rapid injection of an aqueous ammonia borane solution (5 mL and 0.01 g·mL^{-1}) into the flask via a syringe. During the reaction, an electronic balance was employed to monitor the volume of discharged water, which can be further converted into the volume of generated hydrogen to calculate the catalytic activity.

The catalytic test of electrochemical measurements was performed with an electrochemical workstation (CH Instruments electrochemical analyzer, Model CHI760D) in 0.1 M KOH electrolyte. A saturated Ag/AgCl (saturated KCl) electrode was employed as the reference electrode, a graphite rod was employed as the counter electrode. To prepare the working electrode, 1 mL ethanol (Sinopharm Chemical Reagent Co., Ltd., China) was mixed with 30 μL Nafion 5 wt.% solution (DuPont Inc.), followed by the addition of 5 mg catalyst under ultrasonication for at least 60 min to form a homogeneous ink. Then 5 μL of the ink was dropped onto a glassy carbon electrode (GCE) with a diameter of 3 mm, and the as-obtained GCE was dried at ambient conditions under air. Before the test, the electrolyte was degassed by bubbling N_2 for at least 30 min, and the catalysts were activated by 20 cyclic voltammetry (CV) scans from 0 to −0.5 V (vs. RHE) at a scan rate of 100 mV·s^{-1}. Linear sweep voltammetry (LSV) was conducted between −1.27 and −0.57 V (vs. RHE) with a scan rate of 5 mV·s^{-1}. Cyclic voltammetry (CV) tests were conducted between −0.87 and 0.03 V (vs. RHE) with a scan rate of 50 mV·s^{-1}. The electrochemical impedance spectroscopy (EIS) measurements were conducted from 100 kHz to 1 Hz, and the amplitude of the sinusoidal potential signal was 5 mV.

(Steady-state isotopic) transient kinetic analysis

For transient kinetic analysis, as similar to the above, 20 mg catalyst was preloaded in the U-shaped reactor, and subjected to 1.0 vol.% $C^{16}O$ + 20.0 vol.% $^{16}O_2$ in Ar with the flow rate of was 20 mL·min^{-1}. Upon reaching steady-state at 100 °C, the feed gas was switched to a flow of Ar with the same flow rate. After reaching stable, the feed gas was switched to 1.0 vol.% $C^{16}O$ + 20.0 vol.% $^{18}O_2$ in Ar with the flow rate of was 20 mL·min^{-1}. For steady-state isotopic transient kinetic analysis, the feed flow was switched between 1.0 vol.% $C^{16}O$ + 20.0 vol.% $^{16}O_2$ in Ar and 1.0 vol.% $C^{16}O$ + 20.0 vol.% $^{18}O_2$ in Kr with the flow rate of was 20 mL·min^{-1}. The temperature and pressure were kept as 100 °C and 1.85 bar, respectively. The effluent gas stream was monitored by a TILON LC-D200 mass spectrometer (MS).

DFT calculations

All DFT calculations were conducted utilizing the Vienna ab initio simulation package (VASP) with the generalized gradient approximation (GGA) for the electron-electron exchange-correlation function as formulated by Perdew, Burke, and Ernzerhof (PBE), and the projector-augmented wave (PAW) potential for the valence electron-ion interaction[44–46]. We used a cutoff energy of 400 eV for Kohn-Sham orbitals, a Monkhorst-Pack grid for the k-points sampling in the Brillouin zone and a second-order Methfessel-Paxton smearing with a width of 0.05 eV[47]. The Pt_xCo_{13-x} cluster is placed in a 14 × 14 × 14 Å cubic box with periodic boundary conditions, and thus the interaction between the cluster and its periodic image is negligible. A 3 × 3 × 3 Monkhorst–Pack k-point mesh within the surface Brillouin zones was used for these models. In all models, the geometry optimizations were conducted by using a force-based conjugate gradient method. Convergence of saddle points and minima were believed to reach when the maximum force in each degree of freedom was less than 0.03 eV · Å^{-1}. In order to obtain the atomic charges, a fast algorithm operating on a charge density grid was carried out for Bader charge analysis[48,49]. The resultant charge density difference is plotted by using VESTA visualization software.

CMD simulations

Hybrid potential classic molecule dynamic simulations were performed in a constant volume and constant temperature (NVT) ensemble[50] using LAMMPS simulation package[51–53] to simulate the catalyst restructuring, with model construction details provided in the Supplementary Note. Using a hybrid potential approach, we employed accurate interatomic potential second nearest-neighbor modified embedded atom method (MEAM) coupled with charge equilibration (2NNMEAM+Qeq) for Co–O oxidize system[54], the 2NN MEAM formalism for Pt–Co binary systems[55], and a semi-empirical interatomic potential for graphite carbon[56] combined with 12-6 Lennard–Jones (LJ) potentials for other pairs as shown in Table S3. We included two-body LJ potentials with a cutoff distance of 12 Å to describe the interactions among the support, bimetallic nanoparticle, and gas molecules, which can be written as:

$$\phi(r_{ij}) = \frac{q_i q_j}{r_{ij}} + 4\varepsilon_{ij}\left[\left(\frac{\sigma_{ij}}{r_{ij}}\right)^{12} - \left(\frac{\sigma_{ij}}{r_{ij}}\right)^{6}\right] \quad (1)$$

After energy minimization, the system is initialized at a temperature of 300 K, ensuring that the velocities of the atoms conform to a Gaussian distribution. Subsequently, the system temperature was initially at 300 K for 1000 ps using Nosé-Hoover thermostat[50] with a time step of 0.25 fs, and then increased rapidly at a rate of 8 K/ps until it reached target temperature 700 K. Subsequently, a 0.5 fs time step for 2×10^6 iterations was applied at 700 K using the Berendsen thermostat with a 100 fs damping constant. The initial distance between particle and its images was approximately 25.4 Å. This distance is deliberately larger than the chosen van der Waals long-range cutoff (12.0 Å) to avoid long-range interactions[57]. Moreover, the shortest distance between particle and its images during the simulation was approximately 12.2 Å, and still larger than the cutoff of 12.0 Å.

Data availability

The authors declare that all the important data to support the findings in this paper are available within the main text or in the Supplementary information. Extra data are available from the corresponding author upon request.

References

1. Ma, Y. et al. Reactant enrichment in hollow void of Pt NPs@MnO_x nanoreactors for boosting hydrogenation performance. *Natl Sci. Rev.* **10**, nwad201 (2023).
2. Zhang, H., Jin, M. & Xia, Y. Enhancing the catalytic and electrocatalytic properties of Pt-based catalysts by forming bimetallic nanocrystals with Pd. *Chem. Soc. Rev.* **41**, 8035–8049 (2012).
3. Xu, Y. & Zhang, B. Recent advances in porous Pt-based nanostructures: synthesis and electrochemical applications. *Chem. Soc. Rev.* **43**, 2439–2450 (2014).
4. Yu, W., Porosoff, M. D. & Chen, J. G. Review of Pt-based bimetallic catalysis: from model surfaces to supported catalysts. *Chem. Rev.* **44**, 5780–5817 (2013).
5. Shao, Q., Wang, P. T., Zhu, T. & Huang, X. Q. Low dimensional platinum-based bimetallic nanostructures for advanced catalysis. *Acc. Chem. Res.* **52**, 3384–3396 (2019).
6. Zhang, B. W., Yang, H. L., Wang, Y. X., Dou, S. X. & Liu, H. K. A comprehensive review on controlling surface composition of Pt-based bimetallic electrocatalysts. *Adv. Energy Mater.* **8**, 1703597 (2018).
7. Fan, J. et al. Recent progress on rational design of bimetallic Pd based catalysts and their advanced catalysis. *ACS Catal.* **10**, 13560–13583 (2020).
8. Xie, C. et al. Surface and interface control in nanoparticle catalysis. *Chem. Rev.* **120**, 1184–1249 (2019).
9. Shi, X. et al. Dynamics of heterogeneous catalytic processes at operando conditions. *JACS Au* **1**, 2100–2120 (2021).
10. Lee, J. D. et al. Dilute alloys based on Au, Ag, or Cu for efficient catalysis: From synthesis to active sites. *Chem. Rev.* **122**, 8758–8808 (2022).
11. Ferrando, R., Jellinek, J. & Johnston, R. L. Nanoalloys: From theory to applications of alloy clusters and nanoparticles. *Chem. Rev.* **108**, 845–910 (2008).

12. Chen, W. et al. Mesokinetics as a tool bridging the microscopic-to-macroscopic transition to rationalize catalyst design. *Acc. Chem. Res.* **55**, 3230–3241 (2022).
13. Luo, L. et al. Tunability of the adsorbate binding on bimetallic alloy nanoparticles for the optimization of catalytic hydrogenation. *J. Am. Chem. Soc.* **139**, 5538–5546 (2017).
14. Nørskov, J. K., Bligaard, T., Rossmeisl, J. & Christensen, C. H. Towards the computational design of solid catalysts. *Nat. Chem.* **1**, 37–46 (2009).
15. Jiao, Y., Zheng, Y., Davey, K. & Qiao, S.-Z. Activity origin and catalyst design principles for electrocatalytic hydrogen evolution on heteroatom-doped graphene. *Nat. Energy* **1**, 16130 (2016).
16. Zhang, Y., Gao, L., Hensen, E. J. M. & Hofmann, J. P. Evaluating the stability of Co_2P electrocatalysts in the hydrogen evolution reaction for both acidic and alkaline electrolytes. *ACS Energy Lett.* **3**, 1360–1365 (2018).
17. Jin, H. et al. Sabatier phenomenon in hydrogenation reactions induced by single-atom density. *J. Am. Chem. Soc.* **145**, 12023–12032 (2023).
18. Xu, H., Fu, Q., Guo, X. & Bao, X. Architecture of Pt-Co bimetallic catalysts for catalytic CO oxidation. *ChemCatChem* **4**, 1645–1652 (2012).
19. Li, H., Yu, X., Tu, S. T., Yan, J. & Wang, Z. Catalytic performance and characterization of Al_2O_3-supported Pt-Co catalyst coatings for preferential CO oxidation in a micro-reactor. *Appl. Catal. A* **387**, 215–223 (2010).
20. Wang, S. et al. Aqueous solution synthesis of Pt–M (M = Fe, Co, Ni) bimetallic nanoparticles and their catalysis for the hydrolytic dehydrogenation of ammonia borane. *ACS Appl. Mater. Inter.* **6**, 12429–12435 (2014).
21. Wang, Q. et al. Dramatic synergy in CoPt nanocatalysts stabilized by "click" dendrimers for evolution of hydrogen from hydrolysis of ammonia borane. *ACS Catal.* **9**, 1110–1119 (2018).
22. Zhang, J. et al. Synergistic effects in atomic-layer-deposited PtCox/CNTs catalysts enhancing hydrolytic dehydrogenation of ammonia borane. *Appl. Catal. B: Environ.* **235**, 256–263 (2018).
23. Wei, M. et al. Highly efficient Pt-Co alloy hollow spheres with ultra-thin shells synthesized via Co-BO complex as intermediates for hydrogen evolution reaction. *J. Catal.* **381**, 385–394 (2020).
24. Yang, W. et al. Tuning the cobalt–platinum alloy regulating single-atom platinum for highly efficient hydrogen evolution reaction. *Adv. Funct. Mater.* **32**, 2205920 (2022).
25. Chen, Q. et al. Excavated octahedral Pt-Co alloy nanocrystals built with ultrathin nanosheets as superior multifunctional electrocatalysts for energy conversion applications. *Nano Energy* **39**, 582–589 (2017).
26. Núñez, M., Lansford, J. L. & Vlachos, D. G. Optimization of the facet structure of transition-metal catalysts applied to the oxygen reduction reaction. *Nat. Chem.* **11**, 449–456 (2019).
27. Ma, Z. et al. Enhancing oxygen reduction activity of Pt-based electrocatalysts: from theoretical mechanisms to practical methods. *Angew. Chem. Int. Ed.* **59**, 18334–18348 (2020).
28. Wang, H. & Lu, J. A review on particle size effect in metal-catalyzed heterogeneous reactions. *Chin. J. Chem.* **38**, 1422–1444 (2020).
29. Vogt, C. & Weckhuysen, B. M. The concept of active site in heterogeneous catalysis. *Nat. Rev. Chem.* **6**, 89–111 (2022).
30. Wang, X., Liu, Y. & Liang, X. Hydrogenolysis of 5-hydroxymethylfurfural to 2, 5-dimethylfuran over supported Pt-Co bimetallic catalysts under mild conditions. *Green. Chem.* **20**, 2894–2902 (2018).
31. Han, C. et al. Novel PtCo alloy nanoparticle decorated 2D g-C_3N_4 nanosheets with enhanced photocatalytic activity for H_2 evolution under visible light irradiation. *J. Mater. Chem. A* **3**, 23274–23282 (2015).
32. Dohade, M. G. & Dhepe, P. L. Efficient hydrogenation of concentrated aqueous furfural solutions into furfuryl alcohol under ambient conditions in presence of PtCo bimetallic catalyst. *Green. Chem.* **19**, 1144–1154 (2017).
33. Lai, F. J. et al. Architecture of bimetallic Pt_xCo_{1-x} electrocatalysts for oxygen reduction reaction as investigated by X-ray absorption spectroscopy. *J. Phys. Chem. C.* **113**, 12674–12681 (2009).
34. Kong, K. J., Choi, Y. M., Ryu, B. H., Lee, J. O. & Chang, H. J. Investigation of metal/carbon-related materials for fuel cell applications by electronic structure calculations. *Mater. Sci. Eng., C.* **26**, 1207–1210 (2006).
35. Okamoto, H. Co-Pt (cobalt-platinum). *J. Phase Equilib.* **22**, 591 (2001).
36. Becknell, N., Zheng, C., Chen, C., Yu, Y. & Yang, P. Synthesis of $PtCo_3$ polyhedral nanoparticles and evolution to Pt_3Co nanoframes. *Surf. Sci.* **648**, 328–332 (2016).
37. Schulenburg, H. et al. Heat-treated PtCo nanoparticles as oxygen reduction catalysts. *J. Phys. Chem. C.* **113**, 4069–4077 (2009).
38. Lanyon, M. A. H. & Trapnell, B. M. W. The interaction of oxygen with clean metal surfaces. *Proc. R. Soc. Lond., Ser. A* **227**, 387–399 (1955).
39. Song, Y. et al. Bimetallic synergy from a reaction-driven metal oxide–metal interface of Pt–Co bimetallic nanoparticles. *ACS Catal.* **13**, 13777–13785 (2023).
40. Chen, W. et al. Reaction mechanism and kinetics for hydrolytic dehydrogenation of ammonia borane on a Pt/CNT catalyst. *AIChE J.* **63**, 60–65 (2017).
41. Chen, W. et al. Synergistic Pt-WO_3 dual active sites to boost hydrogen production from ammonia borane. *iScience* **23**, 100922 (2020).
42. Kuang, P., Ni, Z., Zhu, B., Lin, Y. & Yu, J. Modulating the d-band center enables ultrafine pt_3fe alloy nanoparticles for pH-universal hydrogen evolution reaction. *Adv. Mater.* **35**, 2303030 (2023).
43. Zhang, C. et al. H_2 in situ inducing strategy on Pt surface segregation over low Pt doped $PtNi_5$ nanoalloy with superhigh alkaline HER activity. *Adv. Funct. Mater.* **31**, 2008298 (2021).
44. Kresse, G. & Furthmüller, J. Efficient iterative schemes for ab initio total-energy calculations using a plane-wave basis set. *Phys. Rev. B: Condens. Matter Mater. Phys.* **54**, 11169–11186 (1996).
45. Perdew, J. P., Burke, K. & Ernzerhof, M. Generalized gradient approximation made simple. *Phys. Rev. Lett.* **77**, 3865–3868 (1996).
46. Kresse, G. & Joubert, D. From ultrasoft pseudopotentials to the projector augmented-wave method. *Phys. Rev. B: Condens. Matter Mater. Phys.* **59**, 1758–1775 (1999).
47. Methfessel, M. P. A. T. & Paxton, A. T. High-precision sampling for Brillouin-zone integration in metals. *Phys. Rev. B* **40**, 3616–3621 (1989).
48. Bader, R. F. W. A quantum theory of molecular structure and its applications. *Chem. Rev.* **91**, 893–928 (1991).
49. Henkelman, G., Arnaldsson, A. & Jónsson, H. A fast and robust algorithm for bader decomposition of charge density. *Comput. Mater. Sci.* **36**, 354–360 (2006).
50. Nosé, S. A molecular dynamics method for simulations in the canonical ensemble. *Mol. Phys.* **100**, 191–198 (2002).
51. Thompson, A. P. et al. LAMMPS-a flexible simulation tool for particle-based materials modeling at the atomic, meso, and continuum scales. *Comput. Phys. Commun.* **271**, 108171 (2022).
52. Plimpton, S. J. Fast parallel algorithms for short-range molecular dynamics. *Comput. Phys.* **117**, 1–19 (1995).
53. Aktulga, H. M., Fogarty, J. C., Pandit, S. A. & Grama, A. Y. Parallel reactive molecular dynamics: numerical methods and algorithmic techniques. *Parallel Comput* **38**, 245–259 (2012).
54. Lee, E., Lee, K. R. & Lee, B. J. An interatomic potential for the Li-Co-O ternary system. *Comput. Mater. Sci.* **142**, 47–58 (2018).
55. Kim, J. S. et al. Second nearest-neighbor modified embedded-atom method interatomic potentials for the Pt-M (M = Al, Co, Cu, Mo, Ni, Ti, V) binary systems. *Calphad* **59**, 131–141 (2017).
56. Lee, B. J. & Lee, J. W. A modified embedded atom method interatomic potential for carbon. *Calphad* **29**, 7–16 (2005).

57. Kaminski, S., Daminelli, G. & Mroginski, M. A. Molecular dynamics simulations of the chromophore binding site of Deinococcus radiodurans bacteriophytochrome using new force field parameters for the phytochromobilin chromophore. *J. Phys. Chem. B* **113**, 945–958 (2009).

Acknowledgements

This work was financially supported by the National Key R&D Program of China (2021YFA1501403), the Natural Science Foundation of China (22038003, 22178100, 22178101, and U22B20141), the Shanghai Pilot Program for Basic Research (22TQ1400100-15), the Innovation Program of Shanghai Municipal Education Commission, the Program of Shanghai Academic/Technology Research Leader (21XD1421000), the Shanghai Science and Technology Innovation Action Plan (22JC1403800). The authors thank the staff members from the BL11B and BL20U beamline of Shanghai Synchrotron Radiation Facility (SSRF) for assistance during data collection.

Author contributions

X.D., C. Lian, and X.L. conceived this work. W.C., Y.S., C. Liu, and Z.R. performed the experiments, collected the data, and wrote the paper. Z.H., Z.C., and X. Zhang conducted the density-functional theory calculation and molecular dynamic simulations. S.L., L.X., J.Z., G.Q., X. Zhou, D.C., and W.Y. helped with data analyzes and discussions.

Competing interests

The authors declare no competing interests.

Additional information

Supplementary information The online version contains supplementary material available at https://doi.org/10.1038/s41467-024-53474-0.

Correspondence and requests for materials should be addressed to Cheng Lian, Xi Liu or Xuezhi Duan.

Peer review information *Nature Communications* thanks the anonymous reviewer(s) for their contribution to the peer review of this work. A peer review file is available.

Reprints and permissions information is available at http://www.nature.com/reprints